Modeling and estimation problems in the visuomotor pathway

Bijoy K. Ghosh, *Fellow, IEEE*, Wenxue Wang, *Member, IEEE*, Zachary V. Freudenburg

Abstract

In this chapter we describe how a population of neurons model the dynamic activity of a suitable region of the visual cortex, responding to a class of visual inputs. Specifically, a large scale neuronal model has been described which generates a propagating wave of activity that has been independently recorded in experiments using multiple electrodes and voltage sensitive dyes. We show how the model cortex is able to discriminate location of target in the visual space. The discrimination is carried out using two separate algorithms. The first method utilizes statistical detection wherein the activity waves generated by the visual cortex are encoded using principal components analysis. The representation is carried out, first in the spatial domain and subsequently in the temporal domain over a sequence of sliding windows. Using the model cortex, we show that the representation of the activity waves, viewed as a 'beta strand', is sufficiently different from each other for alternative locations of point targets in the visual space. Discrimination is carried out assuming that the noise is additive and Gaussian. In the second method, the beta strands are discriminated using a nonlinear dynamical system with multiple regions of attraction. Each beta strand corresponds to a suitable initialization of the dynamical system and the states of attraction correspond to various target locations. The chapter concludes with a discussion of the motor control problem and how the cortical waves play a leading role in actuating movements that would track a moving target with some level of evasive maneuvers.

Index Terms

Cortex Model, Statistical Detection, Hypothesis Testing, Nonlinear Dynamics, Kuramoto Model.

B. K. Ghosh and W. Wang are in the Department of Mathematics and Statistics, Texas Tech University, Lubbock, TX, USA. Z. V. Freudenburg is in the Department of Computer Science and Engineering, Washington University in St. Louis, MO, USA.

This work is partially supported by NSF grant EIA-0218186 and NSF grant ECS-0323693.

I. INTRODUCTION

In this chapter our goal is to describe modeling and estimation problems that arise in the animal visuomotor pathway. The pathway is particularly adept in tracking targets that are moving in space, acquire and internally represent images of the target and finally actuate a suitable motor action, such as capturing the target. In Fig. 1 we show the tracking maneuver of a freshwater turtle as it strives to capture a moving fish. Turtles anticipate future position of a moving target by solving a motion prediction problem – a task that is believed to be initiated in the visual cortex. Visual inputs to the retina are routed through the geniculate before it hits the cortex (see Fig. 2). The role of the visual pathway prior to the cortex is essentially filtering the visual signal although the role of the cortex is 'somewhat more involved' which we presently describe.

Mammals have a cerebral cortex that embodies several topographically organized representations of visual space. Extracellular recordings show that neurons in a restricted region of visual cortex are activated when a visual stimulus is presented to a restricted region of the visual space, the classical receptive field of the neuron [7]. Neurons at adjacent points in the cortex are activated by stimuli presented at adjacent regions of the visual space. Consequently, there is a continuous but deformed map of the coordinates of visual space to the coordinates of the cortex. Extracellular recordings from the visual cortex of freshwater turtles produce a different result [16]. Neurons at each cortical locus are activated by visual stimuli presented at every point in the binocular visual space, although the latency and shape of the response waveforms vary as the stimulus is presented at different loci in the visual space. This suggests that there may not be a simple map of the coordinates of the visual space to the coordinates of the visual cortex in turtles. Position in the visual space is perhaps represented in a form other than a retinotopic map. Experiments conducted by Senseman and Robbins [27], [29], [30] have supported this viewpoint. They used voltage sensitive dye methods to show that presentation of a visual stimulus to the retina of an *in vitro* preparation of the turtle eye and brain produces a wave of depolarization that propagates anisotropically across the cortex (see Fig. 3 for a visualization of the wave propagation in a model cortex). These waves have been demonstrated using both multielectrode arrays and voltage sensitive dyes [23], [24], [28]. Both methods detect the activity of populations of pyramidal cells [28]. The waves have been analyzed using a variant of the principal components method, known as Karhunen-Loeve decomposition. Individual waves could

be represented as a weighted sum of as few as three eigenvectors which are functions of the coordinates of the cortex. Interestingly, presentation of different visual stimuli, such as spots of light at different points in the visual space, produce waves that have different representations in the three dimensional eigenspace. This raises the possibility that visual information is coded in the spatiotemporal dynamics of the cortical waves. Subsequent research work has provided abundant evidence that the traveling electrical waves are observed not only in turtle visual cortex [24], but also across olfactory, visual and visuomotor areas of cortex in a variety of species [10].

Propagating waves with comparable properties can be produced in a large scale model of turtle visual cortex that contains geniculate and cortical neurons [9], [20], [21], [32]. The large scale model, described in this chapter, contains geniculate neurons in the dorsal lateral geniculate complex of the thalamus and the five major populations of neurons in the visual cortex (see Fig. 4 for a model cortex). Turtle visual cortex has three layers: an outer layer 1, an intermediate layer 2 and an inner layer 3 and is divided into lateral and medial parts. Pyramidal cells (including lateral and medial pyramidal cells) have somata situated in layer 2 and are the source of efferent projections from the cortex. The cortex also contains at least three populations of inhibitory interneurons, the subpial (situated in the outer half of layer 1), the stellate (situated in the inner half of layer 1) and the horizontal cells (situated in layer 3). Interactions between these five types of cells involve two types of effects: excitatory and inhibitory. Both geniculate and pyramidal cells are excitatory. Geniculate neurons project excitatory contacts onto pyramidal cells, subpial cells and stellate cells. Pyramidal cells give rise to excitatory inputs to the inhibitory interneurons as well as neighbor pyramidal cells. Subpial, stellate and horizontal cells are inhibitory and provide inhibitory inputs to pyramidal cells. Subpial and stellate cells also involve recurrent connections to neighbor cells. Fig. 5A shows the interconnections among the cortical neurons in the large scale cortex model. The five types of cells can be thought of as forming two anatomically defined pathways within the cortex (Fig. 5B). A feed-forward pathway (Fig. 5B, left part) involves the geniculate inputs that make excitatory contacts on subpial, stellate and lateral pyramidal cells. The subpial and stellate cells make inhibitory contacts on the lateral pyramidal cells. Lateral pyramidal cells give rise to excitatory recurrent contacts on the other lateral and medial pyramidal cells. A feedback pathway (Fig. 5B, right part) involves the recurrent collateral of both lateral and medial pyramidal cells, which make excitatory contacts on subpial, stellate and horizontal cells. Each of these populations of inhibitory interneurons make inhibitory

contacts on pyramidal cells. In addition, there are inhibitory contacts between individual subpial cells as well as between individual stellate cells. Both the lateral and medial pyramidal cells give rise to efferent connections to the thalamus, striatum and brainstem.

The retino-cortical pathway has been sketched in Fig. 2. The retinal ganglion cells are densely distributed around a horizontal axis called the 'visual streak'. Thus turtle-vision has a greater acuity across the horizontal axis (along the surface of water for a freely swimming turtle) in comparison to the vertical axis (above and below the water surface). The retinal inputs are redistributed 'retinotopically' on the lateral geniculate nucleus (LGN). The LGN receives feed-forward inputs from the retina and feedback inputs from the cortex. The precise functional role of the LGN is not entirely known and has not been detailed here. Visual input from the LGN to the cortex is not retinotopic. In fact, inputs from the LGN are spatially distributed across the cortex and the axons are shown as lines in Figs. 2, 4 and 6. These lines cross over, giving rise to an intense activity at the rostro-lateral part of the cortex, sparking the generation of a wave.

The visuo-cortical complex is part of an overall visuomotor pathway, sketched in Fig. 7. Visual input converges onto the optic tectum via two separate routes. A direct input from the retina is fused with an input from the cortex at the tectum. The intermediate stages of the cortical input, viz. the striatum, the SN and the PT are not relevant for this paper. The tectum is responsible in predicting future locations of moving targets by processing cortical waves and fusing more recent visual inputs from the retina. The animal is able to make prediction based on long term visual data and correct the prediction based on 'somewhat recent' target location. The exact mechanism of sensor fusion at the tectum is a subject of future research.

II. A Multi-neuronal model of the visual cortex

In this section, we give a description of the large scale model of the turtle visual cortex. Modeling, in general, is an evolutionary process and involves numerous parameters, some of which are obtained by physiological measurements and some of which are simply tuned in the modeling process. For a comprehensive description of the computational model we would like to refer to [21]. Briefly, the dimensions of the somata and dendrites of individual types of neurons are based on measurements from Golgi impregnations of turtle visual cortex [4], [5]. Biophysical parameters for each cell type are measured with *in vivo* intracellular recording methods [14], [15]. The physiology of each type of synapse included in the model is known

from *in vitro* intracellular recording experiments [13]. The kinetics of individual types of voltage gated channels have not been characterized with voltage clamp methods in turtle visual cortex. So the parameters needed to implement Hodgkin-Huxley-like kinetic schemes are obtained from work on mammalian cortex and constrained by comparing the firing patterns of model cells to real cells following intracellular current injections. The geometry of the geniculocortical and intracortical interconnections are known in detail [6], [17]. Moreover, there are some information on the basic shape and dimensions of the axonal arbors of subpial, stellate and horizontal cells from Golgi preparations. These data are used to estimate spheres of influence between subpial, stellate and horizontal cells and their postsynaptic targets.

As noted in the introduction, the visual cortex of freshwater turtles contains three layers. Our model assumes the three layers are projected onto a single plane (see Fig. 4). Each neuron is represented by a multiple compartmental model with 3-29 compartments based on its morphology (see Fig. 8). Each compartment is modeled by a standard membrane equation and implemented in GENESIS [3]. The membrane equation is written using a set of ordinary differential equations described as follows:

$$\begin{aligned}\frac{dV_i(t)}{dt} &= -\frac{1}{C_i}\left[\frac{(V_i(t)-E_r)}{R_i}+\sum_j\frac{(V_i(t)-V_j(t))}{R_{ij}}\right.\\ &\left.+\sum_{ion} g_k(V_i(t)-E_k)+\sum_{syn} g_k(V_i(t)-E_k)+I_{stim}(t)\right] \qquad (1)\end{aligned}$$

where $V_i(t)$ is the time dependent membrane potential of the i^{th} compartment relative to the resting membrane potential, C_i is the total membrane capacitance of the i^{th} compartment, R_i is the total membrane resistance of the i^{th} compartment, and R_{ij} is the coupling resistance between the i^{th} and j^{th} compartments. Total resistances and capacitances are calculated from the geometry of the compartments and the biophysical parameters, R_m, C_m and R_a using standard relationships [3]. The first summation in (1) is over all of the compartments linked to the i^{th} compartment. The second summation is over all of the species of ionic conductances present on the i^{th} compartment. The third summation is over all of the species of synaptic conductances present on the i^{th} compartment. $I_{stim}(t)$ is a time-varying current injected into the i^{th} compartment. The somata are modeled as spherical compartments and the dendrites are modeled as cylindrical compartments. The axons are not modeled as compartments but as delay lines. For a detailed description of compartmental models see [21] and [33]. In Fig. 8 we show the compartmental structures of the

five types of cortical interneurons in the model cortex. Maps of the spatial distribution of neurons in each of the three layers of the cortex are constructed from coronal sections through visual cortex of a turtle. The maps are divided into an 8×56 array of rectangular areas, each measuring $28 \times 190 \mu m$. Experimental data are not available for each of the 8×56 rectangular boxes and are interpolated at locations where measurements are not available. An algorithm is developed in MATLAB to construct an array of neurons in each layer that preserves the ratios of cells between layers in the real cortex. The cells are distributed between 8×56 blocks according to the actual density information. Within each block, the cell coordinates are chosen randomly from a uniform distribution, independently for every block. This algorithm is convenient to use because it can generate as many different models as needed, while retaining the information about the relative densities of cells in the visual cortex of a real turtle. The model in our study has 368 lateral pyramidal cells, 311 medial pyramidal cells, 44 subpial cells, 45 stellate cells and 20 horizontal cells (see Fig. 4). Biophysical data are not available for neurons in the dorsal lateral geniculate complex of turtles, so geniculate neurons are modeled as single iso-potential compartments with a spike generating mechanism. Geniculate axons are modeled as delay lines that extend across the cortex from lateral to medial. The number of geniculate neurons in the model is $L = 201$. The LGN neurons are linearly arranged along the lateral edge of the cortex with axons extending to the cortex (see Fig. 6). The axons of the most rostral (right) and most caudal (left) LGN neurons in the array extend to the caudal and rostral poles of the cortex, respectively. The other afferents[1] are evenly spaced between these two axons. Geniculate afferents enter the cortex at its lateral edge, cross over each other and then run in relatively straight lines from lateral to medial cortex. The rostro-caudal axis of the geniculate is consequently mapped along the caudo-rostral axis of the cortex. The geometry of the geniculate afferents and their spatial distribution are based on anatomical data from [17]. The number of synaptic sites (varicosities) assigned to each geniculate afferent is calculated by multiplying the length of the axon by the average number of varicosities per $100 \mu m$ of axon length. The spatial positions of the individual varicosities (the total of approximately $11,300$ varicosities has been used) are assigned to axons using the distribution of varicosities along the lengths of real axons [17]. The distribution is strongly skewed to the left, indicating a greater number of varicosities in the lateral than in the

[1]An afferent nerve carries impulses toward the central nervous system. The opposite of afferent is efferent

medial part of the visual cortex. For cortico-cortical connections, we have constructed spheres of influence. Therefore, a cortical neuron will be connected to any other cell in the cortex within its sphere of influence. The synaptic strengths are higher in the center of influence and are linearly reduced with the distance. Propagation times between neurons are calculated using the distance between a pair of neurons and conduction velocities. The conduction velocity for geniculate afferents in turtle visual cortex has been measured at $0.18m/s$ [5]. Cortico-cortical connections are given conduction velocities of $0.05m/s$, consistent with measurements of propagating waves in the turtle visual cortex [27], and the conduction velocities for axons of inhibitory interneurons in rat cortex [26].

III. Generation of activity waves in the visual cortex

We have already seen that a group of neurons in the turtle visual cortex has the ability to sustain a traveling wave. Typically this wave results as an interaction between a feed-forward and a feedback circuit (see Fig. 5), the details of which have been explained in [32]. Roughly speaking, the feed-forward circuit controls the origination and propagating speed of the traveling wave and the feedback circuit controls the propagation duration. Waves are typically generated in the pyramidal cells as a result of an external input current that results in an increase in membrane potential. Pyramidal cells locally excite each other, resulting in a region of neural activity which tends to propagate in all directions. Left unabated, these pyramidal cells would excite the entire cortex. Fortunately, the feed-forward circuit incorporates inhibitory actions from the stellate and subpial cells. Although the precise roles of the two inhibitory cells are different and somewhat unclear, they control the timing of wave generation. There are inhibitory actions that inhibit the wave using a feedback circuit due to three different cells: subpial, stellate and horizontal. The feedback inhibition reduces and eventually kills the neuronal activity at the spot where the activity is greatest. The combined effect of the two circuits gives the appearance of a traveling wave. Eventually these waves are killed by a strong gaba (a type of synaptic input) initiated inhibition that originates after a long delay.

Using the large-scale model of the visual cortex that consists of excitatory and inhibitory cells described above, we have observed that the neural population remains hyperpolarized (i.e. maintained a very low membrane potential) long after the initial wave has been killed. The cortex remains unresponsive to future visual inputs, an undesirable property. One way to remedy

this problem is to detect this period of hyperpolarization and increase the synaptic interaction between the excitatory pyramidal cells. This would amplify the tiny input into the pyramidal cells, forcing these cell populations to get out of hyperpolarization. This is achieved successfully, using Hebbian and AntiHebbian adaptation.

In *Hebbian adaptation*, the synaptic strength between two cells increases in proportion to the product of the pre and post synaptic activities. Likewise, in *AntiHebbian adaptation*, the synaptic strength between two cells decreases in proportion to the product of the pre and post synaptic activities. In our model, the excitatory interconnection between pyramidal cells is chosen to be AntiHebbian. This produces increasingly larger synaptic weights between pyramidal cells once the waves have been abated. The inhibitory interactions between the stellate/subpial/horizontal and the pyramidal cells are chosen to be Hebbian. These produce increasingly stronger inhibition to active pyramidal cells (see Fig. 5). In Fig. 9 we show AntiHebbian action on the pyramidal cells. Rows 1a and 2a show wave activity as a function of time. After about 700 ms, the first round of waves has been inhibited and the pyramidal cells are hyperpolarized. The weights between the cells are very large, as indicated by the red lines in the rows 1b and 2b of Fig. 9. A subsequent input causes a second round of waves (not shown in the figure).

In summary, we outline in this section how cortical cells have the ability to generate and maintain a wave of activity. An important result, outlined in this chapter, is that the waves encode target information from the visual scene. We show, using simulation of the model cortex, how Hebbian and AntiHebbian adaptation has been used in generating a series of cortical waves. In later sections we show how these waves encode the location of targets in the visual space. We do not claim to have established a biological role of the Hebbian/AntiHebbian adaptation in the wave generation process observed in actual turtles.

IV. Simulation with a sequence of stationary inputs

The stationary stimulus has been simulated by presenting a 150 ms square current pulse to a set of adjacent geniculate neurons (see Fig. 10). For the purpose of our simulation, 3 equidistant positions of the stimuli have been chosen across the LGN. The stimuli are labeled by ‘Left’, ‘Center’ and ‘Right’ (see Fig. 4), each input goes into 20 LGN neurons, 1–20, 91–110, and 181–200, respectively from left to right along the LGN array. To study the encoding property of the large scale cortex model, noises have been introduced into the model by injecting randomly

generated currents to the somata of cortical neurons that satisfy gaussian distribution. Using waves generated by inputs at different locations in the visual space, we are able to study the encoding property of the model cortex (see [9]).

Without the Hebbian and AntiHebbian adaptation, the model cortex produces propagating waves of activity that last for about 600 ms to 800 ms (see Fig. 3) with stationary inputs described as above. After the wave has propagated, the cortical neurons remain hyperpolarized and unresponsive to any future inputs. In order to study the ability of the model cortex to encode a sequence of consecutive events, the model is expected to generate a sequence of activity waves corresponding to a sequence of visual inputs. In this section we claim that by introducing Hebbian/AntiHebbian adaptation we are able to pull out the model cortex from hyperpolarization after the first wave has propagated.

With the implementation of Hebbian/AntiHebbian adaptation to the model cortex, one obtains a model that responds to the activities of the pyramidal cells by altering intercellular synaptic interactions. Among the many consequences of adaptation, an important one is that the duration of wave propagation is shortened from about 800 ms (see Fig. 3) to less than 400 ms (see Fig. 11). After the end of the first round of waves (around 450 ms in Fig. 11), the synaptic interactions between pyramidal cells are stronger in the case of model cortex with adaptation as compared to the model without adaptation. This results in a strong amplification of tiny inputs into the pyramidal cells, to compensate for the hyperpolarization of membrane potential. An input initiated around 500 ms results in a second wave (see Fig. 11).

The model cortex with adaptation that we describe in this section samples the visual world every 500 ms by producing a wave of cortical activity that lasts for a little less than 400 ms. Each of the 500 ms time interval would be called a period. In the simulations that we have carried out, a target is shown only for the first 150 ms of each period and removed subsequently. A target can be located at three different locations: Left (L), Center (C) or Right (R). At any given period, one would like to detect ‘target location’ from the associated cortical wave observed during the same period. Furthermore, one would like the detection results at any given period be independent of prior locations of the target.

In order to ensure that one period of cortical activity does not ‘spill over’ to the next period, we consider a pair of consecutive periods. In each period a target is located at either ‘L’, ‘C’ or ‘R’. This gives rise to a total of nine pairs of target locations for the two consecutive periods

given by 'LL', 'LC', 'LR', 'CL', 'CC', 'CR', 'RL', 'RC' and 'RR'. Each combination of two locations can be simulated as an input by presenting two 150 ms square current pulses, that start at 0 ms and 500 ms, to the corresponding sets of adjacent geniculate neurons respectively. The overall simulation time is set to 1000 ms. Each of the nine inputs causes the model cortex (with adaptation) to produce a pair of waves of activity in each of the two consecutive periods. Considering a noisy model of the cortex, the simulation is repeated 20 times for each of the nine input pairs giving rise to a set of 180 pairs of activity waves.

The simulation results consisting of membrane potentials of individual neurons are recorded and saved in a data file. Even though the data for all neurons are available, we are primarily interested in the pyramidal neurons and the responses of pyramidal cells are denoted by $I(t,\ n),\ 0 \leq t \leq T,\ 1 \leq n \leq N$ where t is time and n is the index of the pyramidal neuron. The responses of pyramidal neurons are visualized as movies by spatially resampling the data from a nonuniform grid of neuron coordinates to an artificially constructed $l \times l$ uniform grid. The program uses triangle-based linear interpolation, although other methods are also available (triangle-based cubic interpolation, nearest neighbor interpolation, etc) [20]. The interpolated data, for visualization, are denoted by $I(x, y, t)$ where the pair, (x, y), denote the pixels. The value of membrane potential at each pixel is color coded and the spikes are not removed in the process. Selected snapshots from movies corresponding to stationary stimuli (assuming a model cortex without adaptation) are shown in Fig. 3. A comparison between model waves [20] and experimental waves recorded by Senseman [28] show that the two waves have similar features. They originate from the same point in the cortex (rostrolateral edge) and they propagate in both rostrocaudal and mediolateral directions.

The spatiotemporal response $I(x, y, t)$ of the model cortex to different target locations can be viewed as a collection of movie frames (snapshots). Given that every frame has $l \times l$ pixels, and every movie has m frames, it is clear that the dimension of $I(x, y, t)$ could be very high ($l \times l \times m$). In order to compare two movies, in the next section we proceed to describe a principal components based technique. This method has also been used earlier by Senseman and Robbins for the analysis of data recorded from the cortex of a freshwater turtle [29], [30].

Principal components analysis has been introduced independently by many authors at different times. The method is widely used in various disciplines such as image and signal processing, data compression, fluid dynamics, partial differential equations, weather prediction, etc [11]. In

image processing, the method is used for removing a redundancy (decorrelating pixels) from images [25]. The transformation itself is linear, and represents a rotation of a coordinate system, so that neighboring pixels in the new coordinate system are less correlated. Moreover, the rotation proposed by the method is optimal as it leads to a complete removal of the correlation from neighboring pixels, which is equivalent to diagonalizing the image correlation matrix. Consequently, the image can be approximated in a low dimensional subspace, using only selected basis vectors, also called principal eigenvectors. In the theory of partial differential equations, the method is useful for finding a separable approximation to the solution of a partial differential equation, which is optimal in the sense that it maximizes the kinetic energy cost functional [8].

Depending on the context, the method goes by the names: Karhunen-Loeve (KL) decomposition, proper orthogonal decomposition, Hotelling decomposition and singular value decomposition. We shall refer to it as the KL decomposition which has already been applied to the analysis of cortical waves (see [9], [21] [29] [30]). The next section describes some of the main ideas using double KL decomposition.

V. Encoding Cortical Waves with β-Strands using double KL decomposition

In this section, we describe how the set of 180 pairs of activity waves (described in section IV) are encoded, using double KL decomposition, as β-strands. For each of the nine input pairs, the model cortex with adaptation is repeatedly simulated by adding independent and identically distributed Gaussian noises to each of its neurons. As a result of additive noise injected to the cortical neurons, repeated presentation of the same stimulus does not produce the same response in general. We discuss how to utilize a two-step KL decomposition to analyze the cortical responses of the model cortex to various stimuli with injected noises using *sliding detection window* (SDW) technique. As shown in Fig. 12, the time axis is covered by equal-length, overlapping encoding windows and double KL-decomposition is applied to the segment of the spike rate signal that is covered by each window. Both the starting and ending times of the windows change while the length of the window remains constant. Another encoding window technique considered in [9] is the *expanding detection window* (EDW) for which the starting time remains unchanged at 0 ms. In this section we only describe the SDW technique using which each segment of the cortical wave is mapped to a point in a suitably defined B-space. Plotting images of successive windows produce a sequence of points in the B-space, called the

β-strand (see Fig. 15). This is a vector-valued function of time and is an alternative way to encode the original movie as a strand. The encoding process is now described in details.

Prior to the double KL decomposition process, the spike trains from the pyramidal cells are smoothed by a low pass filter into a spike rate function. Fig. 13 shows some examples of spike trains of pyramidal cells and their smoothed spike rates. For a particular input stimulus, we continue to use $I(t,\ n),\ 0 \leq t \leq T,\ 1 \leq n \leq N$ to denote the smoothed spike rate of the cell as a spatio-temporal response signal, where t is time and n is the index of the pyramidal neuron. $I(t,\ n)$ can be viewed as a matrix. The t^{th} row represents the spike rate of each neuron at time t in response to a particular stimulus. The n^{th} column corresponds to the pyramidal neuron n. Let the length of each time window be w and let $I(t,\ n),\ t_1+1 \leq t \leq t_1+w,\ t_1 = 0,\ a,\ 2a,\ \cdots$ be the response signals for different time windows. Here a is the amount of time that the encoding windows slide (see Fig. 12). Let M denote the total number of cortical response movies in response to stimuli in the left, center, and right visual field. For the $k^{th},\ k = 1,\ 2,\ \cdots,\ M$ movie, the spatio-temporal signal in this time window can be viewed as a collection of vectors $\{I^k(t_1+1),\ I^k(t_1+2),\ \cdots,\ I^k(t_1+w)\}$ where $I^k(t_1+i) \in \mathbb{R}^{1\times N},\ i = 1,\ 2,\ \cdots,\ w$. The dimensionality of the cortical response is reduced by two KL transforms into A-space and B-space, respectively. We first describe the KL transform into A-space. The covariance matrix $C_1 \in \mathbb{R}^{N\times N}$ for a family of M movies is calculated as

$$C_1 = \frac{1}{Mw}\sum_{k=1}^{M}\sum_{i=1}^{w}(I^k(t_1+i))^T(I^k(t_1+i)) \tag{2}$$

where $(I^k(t_1+i))^T$ is the transpose of $I^k(t_1+i)$. The matrix C_1 is symmetric and positive semi-definite, so its eigenvalues are all real and non-negative and the corresponding eigenvectors form an orthonormal basis in $\mathbb{R}^N$. The eigenvectors corresponding to the largest p eigenvalues of C_1 are called the principal eigenvectors, or modes, and the p^{th}-order successive reconstruction of the spatio-temporal signal $I^k(t) \in \mathbb{R}^{1\times N}$ is given by

$$\hat{I}^k(t_1+i) = \sum_{j=1}^{p}\alpha_j^k(t_1+i)\,\phi_j^T,\quad i = 1,\ 2,\ \cdots,\ w \tag{3}$$

where $\phi_j \in \mathbb{R}^{N\times 1}$ is the j^{th} principal mode, the time coefficients $\alpha_j^k(t_1+i)$ are given by $\alpha_j^k(t_1+i) = \langle I^k(t_1+i),\ \phi_j^T\rangle$ and $\langle\cdot,\ \cdot\rangle$ stands for the standard inner product. The coefficients $\alpha_j^k(t_1+i)$ of the KL-decomposition are uncorrelated in terms of j and we call $\alpha_j^k(t),\ t_1+1 \leq t \leq t_1+w,\ 1 \leq j \leq p$ the p^{th}-order A-space representation of the movie segment within the

corresponding time window for the k^{th} movie. Fig. 14 shows the first three principal modes and the corresponding time coefficients in a certain time window. The vector function

$$[\alpha_1^k(t),\ \alpha_2^k(t),\ \cdots,\ \alpha_p^k(t)],\ t_1+1 \le t \le t_1+w \tag{4}$$

can be viewed as a sample function of a vector random process. Statistical analysis of a random process can be facilitated if the process is further parameterized using a second KL decomposition. Let

$$\gamma_j^k = \begin{bmatrix} \alpha_j^k(t_1+1) \\ \alpha_j^k(t_1+2) \\ \vdots \\ \alpha_j^k(t_1+w) \end{bmatrix}, \quad (\xi^k)^T = \begin{bmatrix} \gamma_1^k \\ \gamma_2^k \\ \vdots \\ \gamma_p^k \end{bmatrix} \tag{5}$$

where $j = 1,\ 2,\ \cdots,\ p$. Calculating the covariance matrix as in (2), we have

$$C_2 = \frac{1}{M}\sum_{k=1}^{M} (\xi^k)^T(\xi^k). \tag{6}$$

The q^{th}-order successive approximation of the k^{th} vector ξ^k is given by

$$\hat{\xi}^k = \sum_{j=1}^{q} \beta_j^k \psi_j^T \tag{7}$$

where $\psi_j,\ j = 1,\ 2,\ \cdots,\ q$ are the eigenvectors corresponding to the largest q eigenvalues of the matrix C_2. The coefficients β_j^k are found by orthogonal projection of ξ^k onto the j^{th} eigenvector $\beta_j^k = \langle \xi^k,\ \psi_j^T \rangle$. The β vector is referred to as the B-space representation of the cortical movie restricted to a given time window. It turns out that only a few β components capture most of the information contained in the original movie and the rest of the β components are close to zero. Repeating the above data processing procedure for all the sliding encoding windows of a movie produces a β-strand as a vector-valued function of time. We refer to this β-strand as the B-space representation of this movie. By discarding those components that are close to zero, we obtain a low dimensional representation of the original movie segment. If, for each sliding encoding window, the first q components of each β vector are used, we say that the vector consisting of these q components is the q^{th}-order B-space representation of the movie. The statistical mean of the β-strands of the left-, center-, and right-stimuli movies can be easily obtained. In our analysis of this section, we used $w = 10,\ M = 180,\ p = 679,\ q = 3$ and the values of t_1 were chosen to be $0, 2, 4, \cdots$. Fig. 15 shows the mean β-strands for 60 presentations of stimuli at the

left, center, and right clusters of geniculate neurons in the first time period and the second time period respectively.

VI. Statistical detection of position

In this section, the problem of detection is posed as a hypothesis testing problem. Assume that the three positions of the target correspond to three different hypotheses, i.e. let H_1, H_2 and H_3 denote the hypothesis that the stimulus is from the left, center and right, respectively. Let us write

$$r(t) = s_i(t) \ + \ n(t), \ i = 1, \ 2, \ 3 \tag{8}$$

where $n(t)$ represents a vector-valued Gaussian noise process contained in the β-strand with mean 0.

A. Series Expansion of Sample Functions of Random Processes

The β-strand, $r(t)$, can be regarded as a sample function of a vector stochastic process. It is well known that a deterministic waveform with finite energy can be represented in terms of a series expansion. This idea can be extended to include sample functions of a random process as well. In our case, we propose to obtain a series expansion of the β-strand within a chosen detection window. This process involves finding a complete orthonormal set $\{\phi_i(t), \ i \in \mathbf{N}\}$ ($\mathbf{N}$ denotes the set of integers) and expanding $r(t)$ as:

$$r(t) = l.i.m._{L\to\infty} \sum_{i=1}^{L} r_i \phi_i(t), \quad T_1 \le t \le T_2 \tag{9}$$

where $\phi_i(t)$ are vectors of the same dimension as $r(t)$. Let us denote $r^k(t)$ and $\phi_i^k(t)$ to be the k^{th} component of the vectors $r(t)$ and $\phi_i(t)$ respectively. In (9), $l.i.m.$ denotes "limit in the mean" which is defined as

$$\lim_{L\to\infty} E[\sum_{k=1}^{q} (r^k(t) - \sum_{i=1}^{L} r_i \phi_i^k(t))^2] = 0, \quad T_1 \le t \le T_2 \tag{10}$$

where E is the expectation operator. The coefficients r_i, to be defined later in (13), are required to be uncorrelated with each other. This is to say that, if $E[r_i] = m_i$, then we would like to have

$$E[(r_i - m_i)(r_j - m_j)] = \lambda_i \delta_{ij}. \tag{11}$$

The value of r_i^2 has a simple physical interpretation. It corresponds to the *energy* along the coordinate function, $\phi_i(t)$, in a particular sample function. It is shown in [31] that if $m_i = 0$, then λ_i is the *expected* value of the energy along $\phi_i(t)$. Clearly, $\lambda_i \geq 0$ for all i. The complete orthonormal set $\phi_i(t)$ is the solution of the integral equation:

$$\lambda_i \phi_i^k(t) = \sum_{j=1}^{q} \int_{T_1}^{T_2} K_{kj}(t,u)\phi_i^j(u)du \tag{12}$$

where $k = 1,\ 2,\ \cdots,\ q,\quad T_1 \leq t \leq T_2$ and $K(t,\ u)$ is the covariance matrix of the noise process $n(t)$, i.e. $K_{ij}(t,u) = E[n_i(t)n_j(u)]$. Here, t and u denote time and i and j denote indices of the component of the vector noise process. In (12), λ_i is called the eigenvalue of the noise process and $\phi_i(t)$ is called the corresponding eigenfunction. Once the coordinate functions $\{\phi_i(t),\ i \in \mathbf{N}\}$ are obtained, one can project the sample function $r(t),\ T_1 \leq t \leq T_2$ onto $\phi_i(t)$ and obtain the coefficient r_i as

$$r_i = \sum_{k=1}^{q} \int_{T_1}^{T_2} r^k(t)\phi_i^k(t)dt. \tag{13}$$

Let us recall from section V that q is the number of β components we choose for the B-space representation of the cortical movies. The ν^{th}-order representation of $r(t)$ can then be written as a vector $R = [r_1, r_2, \cdots, r_\nu]$.

B. Hypothesis Testing

The proposed detection algorithm is based on computing conditional probability densities and choosing a decision criterion (see [31] for details). Commonly used decision criteria include the Bayes and Neyman-Pearson criteria. In this paper, we use the former for two reasons. The first is that the hypotheses are governed by probability assignments which we denote as $P_j,\ j = 1,\ 2,\ 3$, i.e. hypothesis H_1 occurs with probability P_1, hypothesis H_2 with probability P_2 and hypothesis H_3 with probability P_3. The second reason is that a certain cost is incurred each time an experiment is conducted. We propose to design our decision rule so that *on the average* the cost is as small as possible. It is demonstrated [31] that for a decision using the Bayes criterion, the optimum detection consists of computing the logarithm likelihood ratio and comparing it to a threshold. If we assign the cost of correct detection to be zero and that of a wrong detection

to be 1, the likelihood ratio can be computed (see section 2.3 of [31]) as follows:

$$\Lambda_1(R) = \frac{p_{r|H_2}(R|H_2)}{p_{r|H_1}(R|H_1)} \tag{14}$$

$$\Lambda_2(R) = \frac{p_{r|H_3}(R|H_3)}{p_{r|H_1}(R|H_1)}. \tag{15}$$

The decision regions in the decision space are determined by comparing the logarithm likelihood ratio to the following thresholds:

$$\ln \Lambda_1(R) \underset{H_1 or H_3}{\overset{H_2 or H_3}{\gtrless}} \ln \frac{P_1}{P_2} \tag{16}$$

$$\ln \Lambda_2(R) \underset{H_1 or H_2}{\overset{H_3 or H_2}{\gtrless}} \ln \frac{P_1}{P_3} \tag{17}$$

$$\ln \Lambda_2(R) \underset{H_2 or H_1}{\overset{H_3 or H_1}{\gtrless}} \ln \Lambda_1(R) + \ln \frac{P_2}{P_3}. \tag{18}$$

The associated decision space has been sketched in Fig. 16. For a particular strand $r(t)$, we say that the hypothesis H_1 is true, i.e. the stimulus is from the left part of the visual space, if the logarithm likelihood ratio pair falls in region H_1. Likewise, the same can be said for H_2 and H_3.

In Fig. 16, if $P_1 = P_2 = P_3 = 1/3$, the dividing line between regions H_1 and H_2 becomes the negative vertical axis, the dividing line between regions H_2 and H_3 becomes the diagonal line which is 45 degrees counterclockwise from the positive horizontal axis, and the dividing line between regions H_3 and H_1 becomes the negative horizontal axis. In the following discussion, we assume that $P_1 = P_2 = P_3 = 1/3$. The vector noise process $n(t)$ in (8) could be either white or colored and we address only the case for which $n(t)$ is white.

C. Decoding with Additive Gaussian White Noise Model

If the vector noise process is Gaussian and white, i.e. $E[n(t)n^T(u)] = N_0 I\delta(t-u)$, where $N_0 \in \mathbb{R}$, I is the identity matrix, and $\delta(\cdot)$ is the Dirac function, the eigenfunctions of the noise process turn out to be the orthonormalization of $\{s_i(t),\ i = 1,\ 2,\ 3\}$. So, instead of solving the integral equation (12), we apply the Gram-Schmidt orthogonalization procedure on

$\{s_i(t),\ i=1,\ 2,\ 3\}$ to get $\{\phi_i(t),\ i=1,\ 2,\ 3\}$ as

$$\begin{aligned}\phi_1(t) &= s_1(t)/\text{norm}(s_1(t))\\ \phi_2(t) &= \psi_2(t)/\text{norm}(\psi_2(t))\\ \phi_3(t) &= \psi_3(t)/\text{norm}(\psi_3(t))\end{aligned}$$

where

$$\begin{aligned}\psi_2(t) &= s_2(t) - c_1 * \phi_1(t)\\ \psi_3(t) &= s_3(t) - c_2 * \phi_1(t) - c_3 * \phi_2(t)\\ c_1 &= \text{IP}(s_2(t), \phi_1(t))\\ c_2 &= \frac{\begin{vmatrix}\text{IP}(s_3(t),\phi_1(t)) & \text{IP}(\phi_2(t),\phi_1(t))\\ \text{IP}(s_3(t),\phi_2(t)) & \text{IP}(\phi_2(t),\phi_2(t))\end{vmatrix}}{\begin{vmatrix}\text{IP}(\phi_1(t),\phi_1(t)) & \text{IP}(\phi_2(t),\phi_1(t))\\ \text{IP}(\phi_1(t),\phi_2(t)) & \text{IP}(\phi_2(t),\phi_2(t))\end{vmatrix}}\\ c_3 &= \frac{\begin{vmatrix}\text{IP}(\phi_1(t),\phi_1(t)) & \text{IP}(s_3(t),\phi_1(t))\\ \text{IP}(\phi_1(t),\phi_2(t)) & \text{IP}(s_3(t),\phi_2(t))\end{vmatrix}}{\begin{vmatrix}\text{IP}(\phi_1(t),\phi_1(t)) & \text{IP}(\phi_2(t),\phi_1(t))\\ \text{IP}(\phi_1(t),\phi_2(t)) & \text{IP}(\phi_2(t),\phi_2(t))\end{vmatrix}}\end{aligned}$$

and $\text{IP}(\cdot,\cdot)$ and $\text{norm}(\cdot,\cdot)$ are defined respectively as

$$\begin{aligned}\text{IP}(a(t),b(t)) &= \sum_{k=1}^{q}\int_{T_1}^{T_2} a^k(t)b^k(t)dt\\ \text{norm}(a(t)) &= \sqrt{\text{IP}(a(t),a(t))}.\end{aligned}$$

The remaining $\phi_i(t)$ consist of an arbitrary orthonormal set whose members are orthogonal to $\phi_1(t)$, $\phi_2(t)$, $\phi_3(t)$ and are chosen so that the entire set is complete. We then project $r(t)$ onto this set of orthonormal coordinate functions to generate coefficients r_i as in (13). All of the r_i except $r_1,\ r_2,\ r_3$ do not depend on which hypothesis is true and are statistically independent of $r_1,\ r_2,\ r_3$. The mean values of $r_1,\ r_2,\ r_3$ depend on which hypothesis is true: $E[r_i|H_j] = m_{ij},\ i,j=1,\ 2,\ 3$. Note also that the coefficients $r_1,\ r_2,\ r_3$ are uncorrelated with

each other. Based on the Gaussian assumption, the logarithm likelihood ratio (14) and (15) can be calculated as

$$\begin{aligned}\ln \Lambda_1(R) &= \sum_{i=1}^{3} \frac{1}{N_0}(r_i m_{i2} - \frac{1}{2}m_{i2}^2 - r_i m_{i1} + \frac{1}{2}m_{i1}^2) \\ \ln \Lambda_2(R) &= \sum_{i=1}^{3} \frac{1}{N_0}(r_i m_{i3} - \frac{1}{2}m_{i3}^2 - r_i m_{i1} + \frac{1}{2}m_{i1}^2).\end{aligned}$$

In this study, the length of the sliding detection window has been set to 99 ms. The waves generated in each of the time periods have been used to detect the location of the target at that time period. In Fig. 17, we show the decision spaces for a set of five different time windows chosen from two consecutive time periods. The column in the left corresponds to the first period and the column in the right corresponds to the second period. The noise $n(t)$ is assumed to be additive, white, Gaussian and independent over time.

For each of the decision spaces in Fig. 17, each point on the decision space represents a given cortical wave (restricted to the corresponding time window) in response to an unknown stimulus. The actual position of the stimuli at left, center and right cluster of geniculate neurons are encoded by the blue, red and green colors, respectively. Ideally, any point corresponding to a left, center, or right stimulus should fall in the region of H_1, H_2, or H_3, respectively on the decision space. Any point that does not fall in its corresponding region in the decision space produces a detection error. In Fig. 18, we have plotted the detection error probability as a function of the location of the 'time window'. We observe that the detection error increases slightly when the detection window slides to the latter part of any period. This indicates that the target locations are 'less detectable' towards the latter part of the period in comparison to the earlier part, an observation that has already been made by Du et al. [9]. We also note that the detection error probabilities are slightly higher for the second time period in comparison to the first indicating the 'spill over effect' from the first time period. This phenomenon has not been studied in details in this chapter and will be described in future.

VII. Detection using nonlinear dynamics

The purpose of this section is to introduce yet another computing paradigm, emerging from a network of oscillators, for the purpose of decoding from cortical waves. Elements of the oscillator network interact with each other via phases rather than amplitudes; memorized

patterns correspond to synchronized states. Each unit of the oscillator network oscillates with the same frequency and a prescribed phase relationship. For pattern recognition with a network of oscillators, phase differences, instead of phases, play a crucial role. The mechanism of recognition is related to phase locking. To illustrate the main idea, we would like to review a model proposed by Kuramoto [12].

A. Phase Locking with a network of Kuramoto Models

Consider a dynamical system of the form

$$\dot{\phi}_i = \omega + \sum_{j=1}^{N} s_{ij} \sin(\phi_j - \phi_i + \psi_{ij}) \tag{19}$$

where ϕ_i, $i = 1, \cdots, N$ (assume $N = 2$ for illustration), are phase variables taking values in the interval $[-\pi, \pi)$. The parameters s_{ij} and ψ_{ij} are assumed to satisfy $s_{ij} = s_{ji}$, $\psi_{ij} = -\psi_{ji}$. The index i, refers to the i^{th} unit and these units are coupled. In order to understand the dynamics of (19), we define a new variable $\phi = \phi_1 - \phi_2$ and rewrite (19) as follows

$$\dot{\phi} = -2s_{12} \sin(\phi - \psi_{12}). \tag{20}$$

The stationary points of (20) are given by $\phi - \psi_{12} = k\pi$, out of which the stable points are given precisely by

$$\phi - \psi_{12} = 2k\pi, \quad k = 0, \pm 1, \pm 2, \cdots \tag{21}$$

For ϕ_1, ϕ_2 in the interval $[-\pi, \pi)$, $\phi = \psi_{12}$ and $\phi = \psi_{12} + 2\pi$ are the two stable points if $\psi_{12} < 0$, and $\phi = \psi_{12}$ and $\phi = \psi_{12} - 2\pi$ are the two stable points if $\psi_{12} > 0$. Up to mod 2π, the two stable points of ϕ are actually the same indicating that (20) converges globally to an unique equilibrium point.

B. Memory with two elements

Let us discuss the problem of detecting n patterns with a Kuramoto model using two units (i.e. N=2). In order to use (20) for the purpose of memorizing n patterns, we would require that it has (at least) n equilibria. This can be achieved by rescaling the phase variables as

$$\bar{\phi}_1 = \frac{1}{n}\phi_1, \quad \bar{\phi}_2 = \frac{1}{n}\phi_2.$$

Rewriting (19) with respect to the new variables, we obtain

$$\dot{\bar{\phi}}_1 = \frac{1}{n}\omega + \frac{1}{n}s_{12}\sin(n\bar{\phi}_2 - n\bar{\phi}_1 + \psi_{12})$$
$$\dot{\bar{\phi}}_2 = \frac{1}{n}\omega + \frac{1}{n}s_{21}\sin(n\bar{\phi}_1 - n\bar{\phi}_2 + \psi_{21}).$$

By defining $\bar{\phi} = \bar{\phi}_1 - \bar{\phi}_2$, we obtain analogously the following equation

$$\dot{\bar{\phi}} = -\frac{2}{n}s_{12}\sin(n\bar{\phi} - \psi_{12}). \tag{22}$$

Up to mod 2π, the n stable stationary points of (22) are given by $\bar{\phi}_k^e = \frac{\psi_{12}}{n} + \frac{2(k-1)\pi}{n}$ if $\psi_{12} < 0$. Additionally it can be verified that if

$$\bar{\phi}_k^e - \frac{\pi}{n} < \bar{\phi}(0) < \bar{\phi}_k^e + \frac{\pi}{n}, \tag{23}$$

then $\bar{\phi}(t)$ converges to the k^{th} stable stationary point $\bar{\phi}_k^e$. The phase difference variable $\bar{\phi}(t)$ can be plotted as a unit complex number $e^{i\bar{\phi}(t)}$. In Fig. 19 such a plot is shown when the rescaling parameter n is 3. This gives rise to three stable stationary points at $\bar{\phi}_k^e = \frac{\psi_{12}}{3} + \frac{2(k-1)\pi}{3}$, $k = 1$, 2 and 3.

The main idea behind pattern recognition is to utilize the convergence properties of (22) to distinguish among n complex patterns. Let us define the following n vectors in $\mathbb{C}^2$ as

$$p_1 = \begin{pmatrix} \pi_1 \\ \pi_2 \end{pmatrix} \text{ and } p_k = \begin{pmatrix} e^{+i\frac{(k-1)\pi}{n}}\ \pi_1 \\ e^{-i\frac{(k-1)\pi}{n}}\ \pi_2 \end{pmatrix} \tag{24}$$

for $k = 2,\ 3,\ \cdots,\ n$ where π_1 and π_2 are any two complex numbers such that

$$|\pi_1| = |\pi_2| = 1$$

and

$$arg(\pi_1\bar{\pi}_2) = \frac{\psi_{12}}{n}.$$

The complex vectors p_k, $k = 1, 2, \ldots, n$, are n memorized complex patterns associated with n stable equilibria $\bar{\phi}_k^e, k = 1, 2, \ldots, n$. Let us define a mapping

$$\xi : \mathbb{C}^2 \longrightarrow \mathbb{R} \tag{25}$$

as follows

$$\begin{pmatrix} w_1 \\ w_2 \end{pmatrix} \longmapsto arg(w_1\bar{w}_2).$$

It would follow that $\xi(p_k) = \bar{\phi}_k^e = \frac{\psi_{12}}{n} + \frac{2(k-1)\pi}{n}$. Thus the n patterns p_k, $k = 1, 2, \cdots, n$, are mapped to the n stable equilibria of (22) under the map ξ. Patterns which are close to any p_k would be attracted towards the corresponding k^{th} equilibrium. This principle can therefore be used to recognize between alternative target locations which we would now like to explore.

Target locations are not typically given as a vector of complex numbers. Hence we are not interested in a set of complex patterns. Rather, we would like to memorize patterns of real vectors. Assume that we have n vectors v_k, $k = 1, 2, \cdots, n$, in $\mathbb{R}^Q$ which we would like to memorize. We consider a map

$$T : \mathbb{R}^Q \longrightarrow \mathbb{C}^2 \tag{26}$$

such that

$$v_k \longmapsto p_k, \quad k = 1, 2, \cdots, n$$

where p_k-s are defined as in (24). The memorized patterns are associated with phase difference equilibria via the map ξT where

$$\xi T(v_k) = \bar{\phi}_k^e.$$

The dynamics of (22) can be used to memorize patterns of n real vectors. To detect a pattern v in $\mathbb{R}^Q$, the phase variables ϕ_i-s of the two oscillatory units can be initialized with $\xi T(v)$ and $\bar{\phi}(t)$ converges to one of the equilibria.

As an illustration, a Kuramoto model with 2 units has been chosen to detect the position of visual inputs from the cortical waves generated in the first time period and the second time period respectively. Three equilibria are achieved by rescaling with $n = 3$. The locations of target are detected with the β-strands within a sliding time window of width 99 ms. The average of points on β-strands within the sliding time window in either first or second time period, in $\mathbb{R}^Q$, are mapped to the complex vector space $\mathbb{C}^2$ and the phases of 2 units in the Kuramoto model are initialized. The map T can be either linear or nonlinear. In the case of linear transformation, the map T between the real vector space $\mathbb{R}^Q$ and the complex vector space $\mathbb{C}^2$ is obtained by minimizing the following error criterion

$$\sum_{k=1}^{3} \sum_{j=1}^{60} ||p_k - T q_{kj}|| \tag{27}$$

where k is the position index and j varies over the total number of movies. The vectors p_k-s are defined in (24) and the vectors q_{kj} are average of the β-strands within a time window. In this example, we have $Q = 3$ indicating that only the first three principal components are used for the detection problem. It follows that the rescaled phase difference $\bar{\phi} = \frac{\phi}{3}$ converges to one of the three equilibria that are associated to the three positions of the targets, 'L', 'C' and 'R'. Fig. 20 shows plots of phase difference variable $\bar{\phi}(t)$ in terms of $\sin$ and $\cos$ functions over time for the detection results from 180 cortical responses using the two units Kuramoto model and linear map upon the average points on β-strands within the time window associated the waves in the first time period (left column) and the second period (right column) respectively. The figure shows the detection results within five different sliding time windows. Each curve in Fig. 20 represents a given cortical wave in response to an unknown stimulus. The actual positions of target at left, center and right cluster of geniculate neurons are encoded by blue, red and green colors respectively. Ideally, any curve corresponding to a left, center, or right stimulus should converge to the associated point of equilibria. Any curve that does not approach to its corresponding equilibrium produces a detection error. Performing the detection over a continuum of detection windows and summing the total detection error for each detection window yields the relationship between the probability of detection error and detection window as shown in Fig. 21. It may be remarked that the detection error probabilities are quite large in comparison to Fig. 18 indicating that the algorithm using nonlinear dynamic methods require further improvement.

Since the maps from β-strands to complex vector space is not limited to be linear, one would like to ask if there is a nonlinear map for which the detection results can be improved. In this chapter we give an example of such a map that can improve the detection results using Kuramoto model. We consider the nonlinear map L from the space $\mathbb{R}^Q$ of β-strands to the points on the decision space S, obtained in section VI. Subsequently, we can map the points on the decision space S onto the complex vector space $\mathbb{C}^2$ by a linear transformation D. The maps defined are described as follows:

$$\begin{aligned} L &: \mathbb{R}^Q \longrightarrow S \\ D &: S \longrightarrow \mathbb{C}^2 \end{aligned} \tag{28}$$

The map D is obtained by constructing an optimal linear function that maps each of the three clusters on the decision space S to their corresponding patterns on the complex vector space $\mathbb{C}^2$. The details are similar to optimizing a cost function of the form (27). By concatenating the

two maps L and D we obtain a nonlinear map from the space of β-strands onto the space $\mathbb{C}^2$ of complex patterns. One can now use the Kuramoto model as described earlier. The detection results, shown in Figs. 22 and 23 are considerably improved in comparison to Figs. 20 and 21.

VIII. Role of tectal waves in motor control: A future goal.

We have remarked earlier that an important role of the cortex is in predicting the future locations of a moving target. The turtle tries to track a moving fish by anticipating its future location. We now describe in some details as to how the tracking movement is executed.

In Fig. 7 we show that a turtle is trying to catch a fish that is moving past it from left to right.The turtle first notices the fish at point x_1 at time t_1. It watches the fish until it reaches point x_2 at time t_2, and then moves towards the fish to grasp it with its mouth. However, the fish keeps moving and reaches point x_3 by the time t_3, when the turtle completes its head movement. Thus, the turtle will miss the fish if it bases its head movement on the position of the fish when the movement began. To be successful, the turtle must extrapolate the present position of the fish and plan its head movement to reach point x_3 at time t_3. However, the fish has a stake in the event and will try to evade capture by making escape movements that appear unpredictable to the turtle. An important question in this context is – "How does the turtle accomplish this complex motion extrapolation task?"

The neural system in Fig. 1 is the substrate for the prey capture behavior. A light intensity function, $I(x, y, t)$, contains the image of the moving fish that is the input to the system. The image is transformed by the retinal circuitry and fed, in parallel to the lateral geniculate nucleus and optic tectum. The lateral geniculate transmits information to the cortex, which sends information to the tectum via the striatum, pretectum and substantia nigra. The tectum, thus, receives direct information from the retina with a relatively short time delay and indirect information from the cortex with a longer delay. The tectum contains a topographic map of visual space and can generate a head movement directed towards point x_2 at time t_2. The movement is realized by projections from the tectum to the brain stem reticular formation, which drives the motoneurons that innervate the neck muscles.

An interesting feature of the dynamics of this system is that moving stimuli produce waves of activity in the retina, visual cortex and tectum. Berry et al. [2] used single electrodes to record the responses of retinal ganglion cells in salamanders and rabbits to moving bars. The neural

image of the bar on the retina is a wave of activity that leads the advancing edge of the bar. This phenomenon is due to a contrast gain mechanism in the retinal circuitry and is a potential mechanism underlying motion extrapolation. Wilke et al. [34] used an array of 100 extracellular electrodes to record the responses of ganglion cells in turtles to moving and stationary bars. A moving bar produced a rapid and intense increase in the firing of ganglion cells that was not seen following the presentation of a stationary bar. Several studies [1], [18], [19]) suggest that moving stimuli produce a wave, or 'hill', of activity in the superior colliculus (the mammalian homolog of the optic tectum). More recently, Port et al. [22] recorded simultaneously from pairs of electrodes implanted in the superior colliculus of macaques while the monkeys made visual saccades. Their data suggest that relatively large saccades – typically coordinated with head movements – are accompanied by a wave of activity that proceeds from caudal to rostral across the superior colliculus. They hypothesize that this wave is involved in determining the duration of eye and head movements. Finally, studies using both multielectrode arrays and voltage sensitive dyes (VSDs) show that visual stimuli produce waves of activity in the visual cortex of freshwater turtles [28]. Information about the position and speed of visual stimuli is encoded in the spatiotemporal dynamics of the wave [9], [20]). Both retinal and tectal waves have been considered as candidate mechanisms for motion extrapolation [22], [34]), so it is natural to inquire if they play a role in the turtle's attempt to catch the fish.

Our future work would test the hypothesis that the waves in the visual cortex and optic tectum contain information that can be used to extrapolate the future position of a moving stimulus from its past trajectory. Specifically, we hypothesize that the cortical wave contains information that can be used to extrapolate the future position of a stimulus that has been moving along a smooth trajectory, while the tectal wave contains information that can be used to predict the future position of a stimulus that undergoes an abrupt changes in it's trajectory.

IX. Conclusion

To conclude, we would like to emphasize that the retino-cortical circuit of a turtle has been described in this chapter. The animal scans the visual world by splitting it into a sequence of time windows called 'periods'. In each period, the cortex produces a wave of activity. We emphasize how Hebbian/AntiHebbian adaptation plays a crucial role in maintaining a sequence of cortical activity and describe how these activity waves can be used to decode locations of unknown

targets in space. Two different decoding algorithms have been discussed in this chapter. The first algorithm utilizes a 'Statistical Detection' method to detect the location of a target in the visual space. The proposed method utilizes hypothesis testing by projecting the observed data onto a decision space. The second algorithm is developed using a nonlinear dynamic model that has the ability to converge to an equilibrium point based on where the model has been initialized. Each of the equilibrium points is calibrated with alternative locations of the target and a function is constructed that maps the raw data onto a vector space of complex numbers, that can be used as an initial condition for the model. For the purpose of this chapter, we use the Kuramoto model and construct two different functions that generate the required initial conditions. We show that in order to obtain detection results comparable to that obtained by the 'Statistical Method', a nonlinear function is required to generate the associated initial conditions, and we construct one such function in this chapter. The role of the retino-cortical pathway is discussed in the context of the overall visuomotor control problem and we remark that the tectum plays an important part in the generation of the associated motor commands. Such control problems are the subject of future research.

REFERENCES

[1] R. W. Anderson, E. L. Keller, N. J. Gandhi, and D. Sanjoy. Two-dimensional saccaderelated population activity in superior colliculus in monkey. *J. Neurophysiol.*, 79:2082–2096, 1998.

[2] M. J. II Berry, I. H. Brivanlou, T. A. Jordan, and M. Meister. Anticipation of moving stimuli by the retina. *Nature*, 398:334–338, 1999.

[3] J. M. Bower and D. Beeman. *The Book of Genesis*. TELOS, Santa Clara, 1998.

[4] J. B. Colombe, J. Sylvester, J. Block, and P. S. Ulinski. Subpial and stellate cells: Two populations of interneurons in turtle visual cortex. *J. Comp Neurol*, 471:333–351, 2004.

[5] J. B. Colombe and P. S. Ulinski. Temporal dispersion windows in cortical neurons. *J. Comput Neurosci*, 7:71–87, 1999.

[6] C. E. Cosans and P. S. Ulinski. Spatial organization of axons in turtle visual cortex: Intralamellar and interlamellar projections. *J. Comp. Neurol.*, 296:548–558, 1990.

[7] F. Delcomyn. *Foundations of Neurobiology*. W. H. Freeman & Co., New York, 1998.

[8] M. Dellnitz, M. Golubitsky, and M. Nicol. Symmetry of attractors and the karhunen-loeve decomposition. In L. Sirovich, editor, *Trends and Perspectives in Applied Mathematics*, pages 73–108. Springer Verlag, New York, 1994.

[9] X. Du, B. K. Ghosh, and P. S. Ulinski. Encoding and decoding target locations with waves in the turtle visual cortex. *IEEE Trans. on Biomedical Engineering*, 52:566–577, 2005.

[10] G. B. Ermentrout and D. Kleinfeld. Traveling electrical waves in cortex: Insights from phase dynamics and speculation on computational role. *Neuron*, 29(33-34):33–44, January 2001.

[11] P. Holmes, J. L. Lumley, and G. Berkooz. *Turbulence, Coherent Structure, Dynamical Systems and Symmetry*. Cambridge University Press, Cambridge, 1996.

[12] Y. Kuramoto. *Chemical Oscillations, Waves, and Turbulence*. Springer-Verlag, New York, 1984.

[13] L. J. Larson-Prior, P. S. Ulinski, and N. T. Slater. Excitatory amino acid receptor-mediated transmission in geniculocortical and intracortical pathways within visual cortex. *J. Neurophysiol.*, 66:293–306, 1991.

[14] J. G. Mancilla, M. Fowler, and P. S. Ulinski. Responses of regular spiking and fast spiking cells in turtle visual cortex to light flashes. *Vis Neurosci*, 15:979–993, 1998.

[15] J. G. Mancilla and P. S. Ulinski. Role of $GABA_A$-mediated inhibition in controlling the responses of regular spiking cells in turtle visual cortex. *Vis Neurosci*, 18:9–24, 2001.

[16] P. Z. Mazurskaya. Organization of receptive fields in the forebrain of *Emys orbicularis*. *Neurosci. Behav. Physiol.*, 7:311–318, 1974.

[17] K. A. Mulligan and P. S. Ulinski. Organization of geniculocortical projections in turtles: isoazimuth lamellae in the visual cortex. *J. Comp. Neurol.*, 296:531–547, 1990.

[18] D. P. Munoz, D. Guitton, and D. Pelisson. Control of orienting gaze shifts by the tectoreticulospinal system in the head-free cat. iii. spatiotemporal characteristics of phasic motor discharges. *J. Neurophysiol.*, 66:1642–1666, 1991.

[19] D. P. Munoz and R. H. Wurtz. Saccade-related activity in monkey superior colliculus. ii. spread of activity during saccades. *J. Neurophysiol.*, 73:2334–2348, 1995.

[20] Z. Nenadic, B. K. Ghosh, and P. S. Ulinski. Modeling and estimation problems in the turtle visual cortex. *IEEE Trans. on Biomedical Engineering*, 49:753–762, 2002.

[21] Z. Nenadic, B. K. Ghosh, and P. S. Ulinski. Propagating waves in visual cortex: A large scale model of turtle visual cortex. *J. of Computational Neuroscience*, 14:161–184, 2003.

[22] N. L. Port, M. A. Sommer, and R. H. Wurtz. Multielectrode evidence for spreading activity across the superior colliculus movement map. *J. Neurophysiol.*, 84:344–357, 2000.

[23] J. C. Prechtl, T. H. Bullock, and D. Kleinfeld. Direct evidence for local oscillatory current sources and intracortical phase gradients in turtle visual cortex. In *Proc. Natl. Acad. Sci. USA*, pages 877–882, 2000.

[24] J. C. Prechtl, L. B. Cohen, P. P. Mitra, B. Pesaran, and D. Kleinfeld. Visual stimuli induce waves of electrical activity in turtle cortex. In *Proc. Natl. Acad. Sci. USA*, pages 7621–7626, 1997.

[25] K. R. Rao and P. C. Yip. *The Transform and Data Compression Handbook*. CRC Press, Boca Raton, 2001.

[26] P. A. Salin and D. A. Prince. Electrophysiological mapping of gabaa receptor mediated inhibition in adult rat somatosensory cortex. *J. Neurophysiol.*, 75:1589–1600, 1996.

[27] D. M. Senseman. Correspondence between visually evoked voltage sensitive dye signals and activity recorded in cortical pyramidal cells with intracellular microelectrodes. *Vis. Neurosci.*, 13:963–977, 1996.

[28] D. M. Senseman. Spatiotemporal structure of depolarization spread in cortical pyramidal cell populations evoked by diffuse retinal light flashes. *Vis Neurosci*, 16:65–79, 1999.

[29] D. M. Senseman and K. A. Robbins. Visualizing differences in movies of cortical activity. *IEEE Trans. Visual. Comput. Graphics*, 4:217–224, 1998.

[30] D. M. Senseman and K. A. Robbins. Modal behavior of cortical neural networks during visual processing. *J. Neuroscience*, 19:1–7, 1999.

[31] H. L. Van Trees. *Detection, Estimation and Modulation Theory*. John Wiley and Sons, Inc., New York, 1968.

[32] W. Wang, C. Campaigne, B. K. Ghosh, and P. S. Ulinski. Two cortical circuits control propagating waves in visual cortex. *J. Comput. Neurosci.*, 19:263–289, 2005.

[33] W. Wang, S. Luo, B. K. Ghosh, and P. S. Ulinski. Generation of receptive fields of subpial cells in turtle visual cortex. *J. Integrative Neurosci.*, 5:561–593, 2006.

[34] S. D. Wilke, A. Thiel, C. W. Eurich, M. Greschner, M. Bongard, J. Ammermuller, and H. Schwegler. Population coding of motion patterns in the early visual system. *J. Comp. Physiol. A*, 187:549–558, 2001.

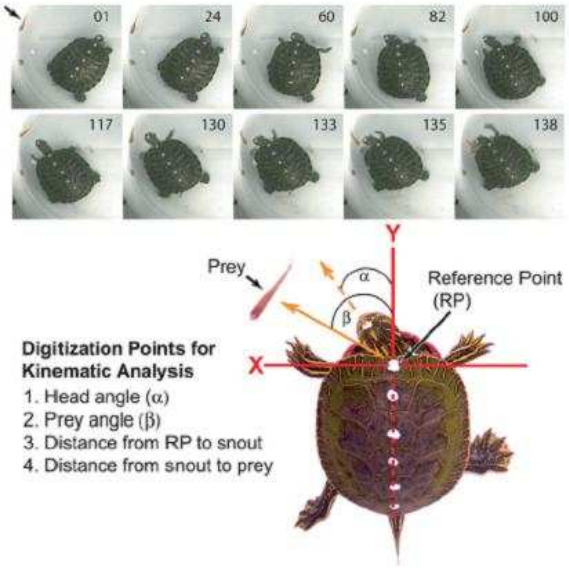

Fig. 1: Kinematic analysis of turtle prey capture. Selected movie frames at the top of the figure show a turtle orienting to a moving fish (arrow) in frame 01 - 82, moving towards it (100 - 130), extending and turning its neck (133 - 135) and capturing the fish (138). The bottom image shows the digitization points of the kinematic analysis.

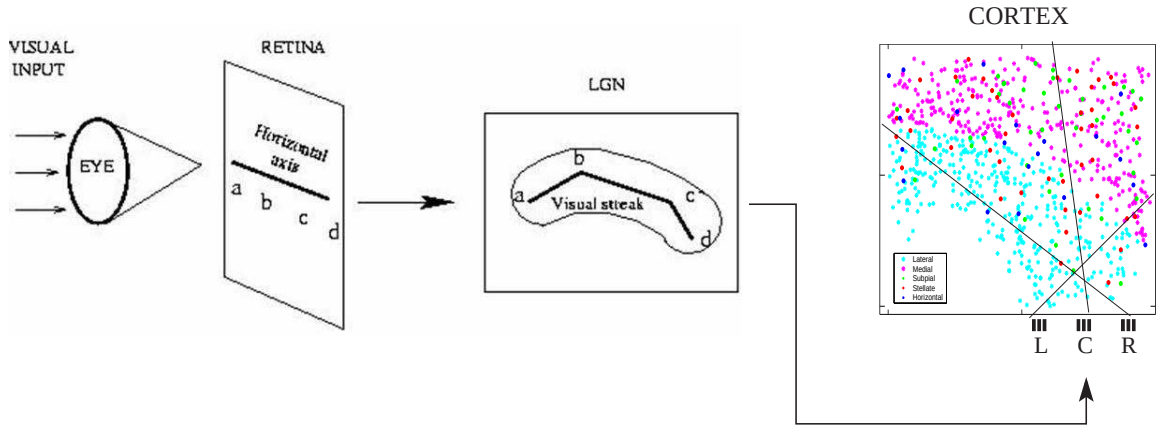

Fig. 2: The Visual Pathway in the turtle visual system from eyes to visual cortex

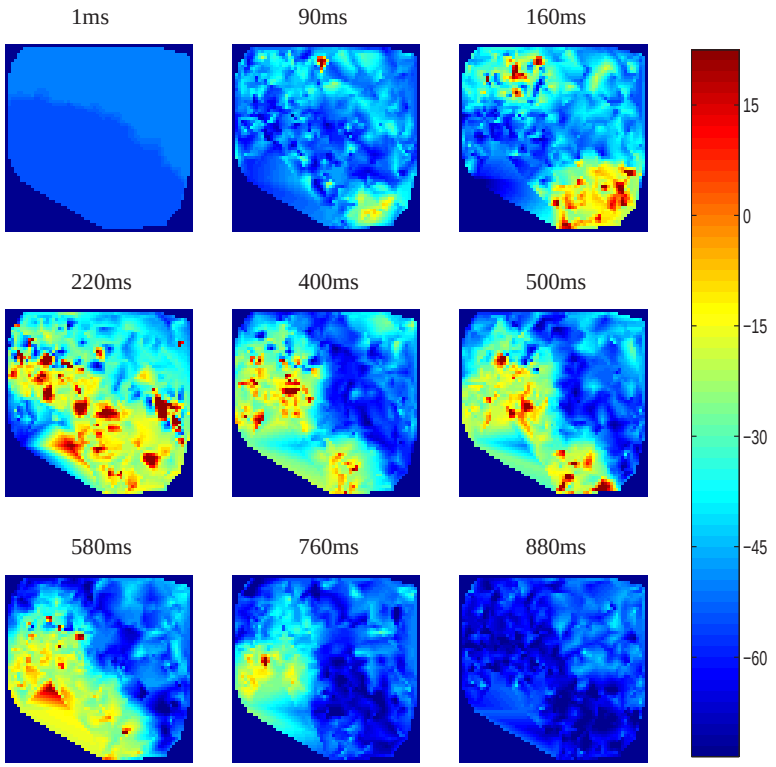

Fig. 3: A traveling wave of cortical activity from the model cortex without Hebbian and AntiHebbian adaptation.

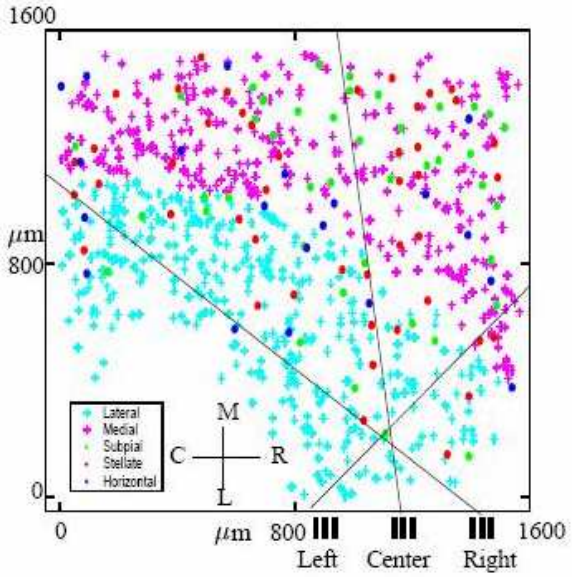

Fig. 4: Distribution of cells in each of the three layers of the turtle cortex projected on a plane. The lateral geniculate (LGN) cells are distributed linearly (shown at the right side of the bottom edge of the cortex) and the solid line shows how they interact with cells in the cortex.

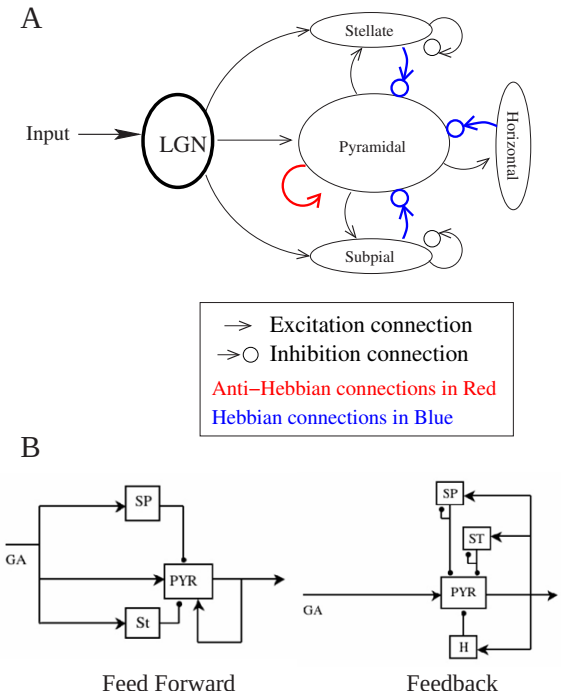

Fig. 5: Cortical circuit of freshwater turtles. Interconnection between neurons in various layers of the visual cortex is shown. Each box symbolizes a population of cells. The geniculate afferents (GA) provide excitatory input to cells in both pathways. The pyramidal cells (PYR) are excitatory. The distinction between medial and lateral pyramidal cells is not made in this diagram. The subpial (SP), stellate (ST) and horizontal (H) cells are inhibitory. The axons of pyramidal cells leave the visual cortex to other cortical areas and to the brainstem in both pathways.

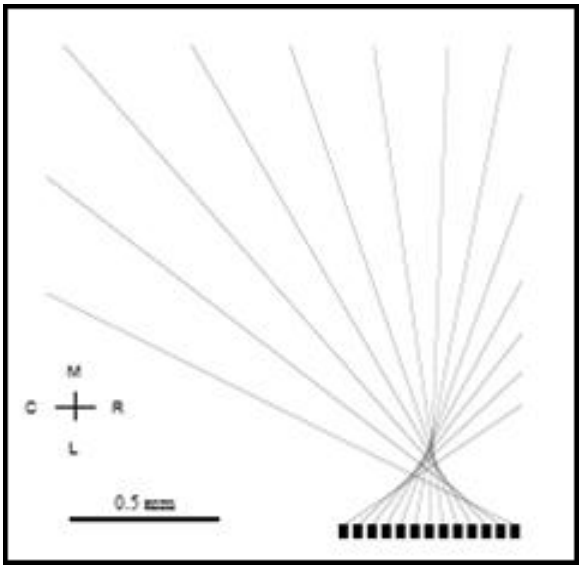

Fig. 6: Linear arrangement of geniculate neurons. The somata are shown as boxes and the corresponding axons are shown as lines. Only 13 out of 201 LGN neurons are shown for clarity.

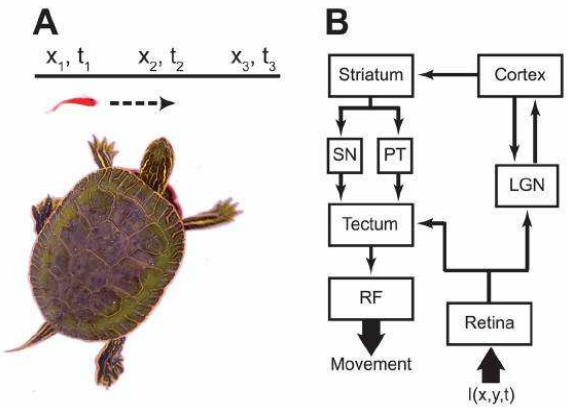

Fig. 7: Prey capture and motion extrapolation. A. To capture a moving fish, a turtle must extrapolate its future position. B. Probable neural substrate for motion extrapolation in turtles. (Abbreviations: LGN, lateral geniculate nucleus; PT, pretectum; RF, reticular formation; SN, substantia nigra).

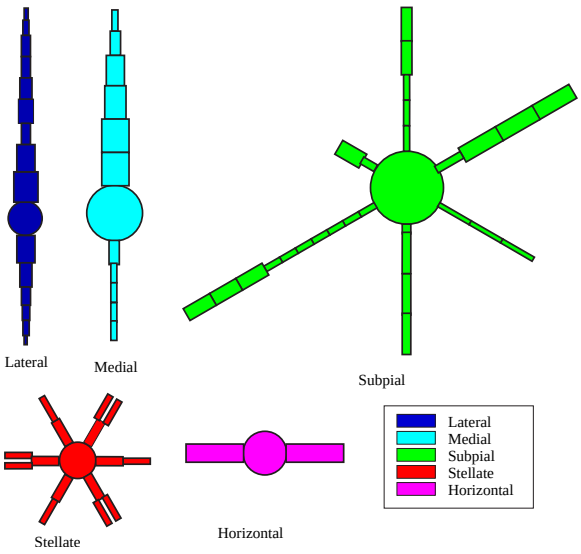

Fig. 8: Compartmental structures of cortical neuron models in the large scale model of turtle visual cortex

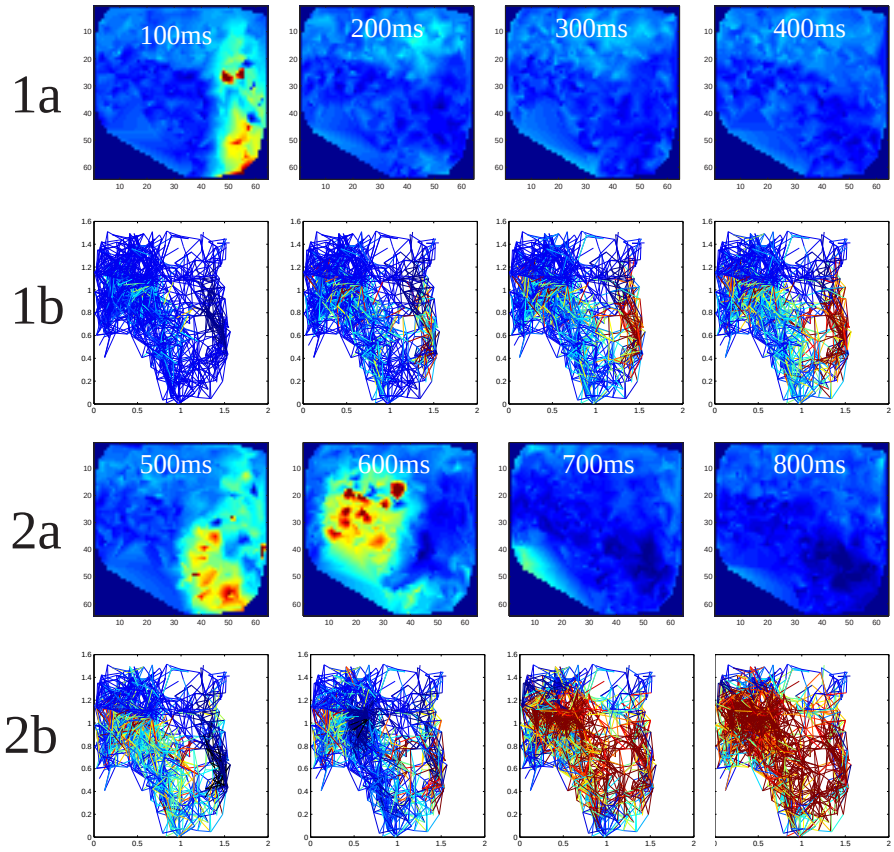

Fig. 9: Pyramidal to pyramidal AntiHebbian synaptic response to changes in the pyramidal activity. (1a): Frames of pyramidal cell activity due to pulse input to the LGN at 0 ms lasting for 150 ms. (1b): Frames of weight responses corresponding to the activities in 1a.(2a): Frames of pyramidal cell activity due to pulse input to the LGN at 400 ms following the first pulse lasting for 150 ms. (2b): Frames of synaptic weight responses corresponding to activities in 2a.

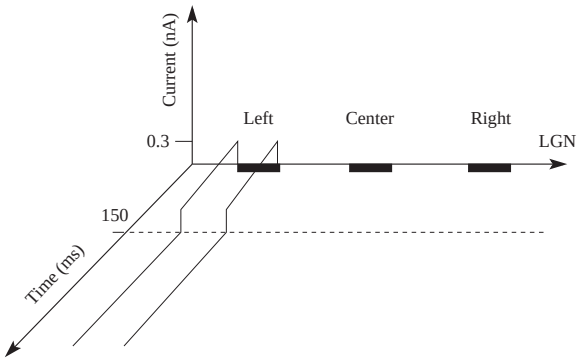

Fig. 10: The Figure shows simulation of flash inputs

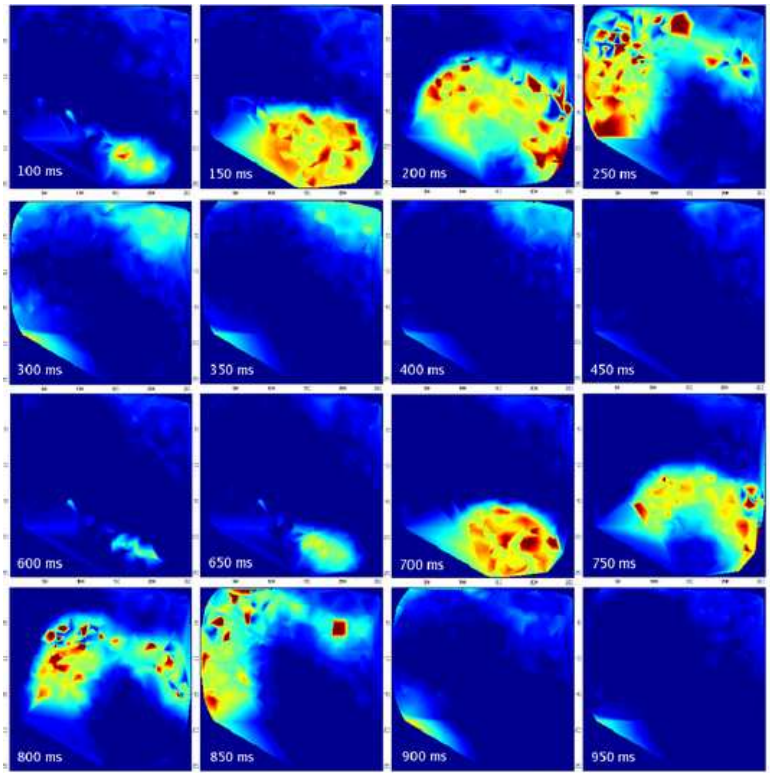

Fig. 11: Two cortical waves generated by the model cortex using Hebbian and AntiHebbian adaptation with two consecutive inputs. The second input is initialized at 500 ms.

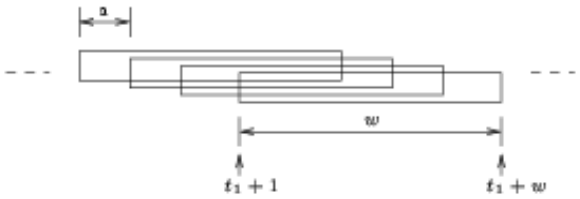

Fig. 12: Encoding window. The time axis is covered by equal-length, overlapping, sliding encoding windows. Both the starting and ending times of the windows slide over the time axis while the length of the window remains constant. a is the amount of time that the window slides and w is the width of each encoding window.

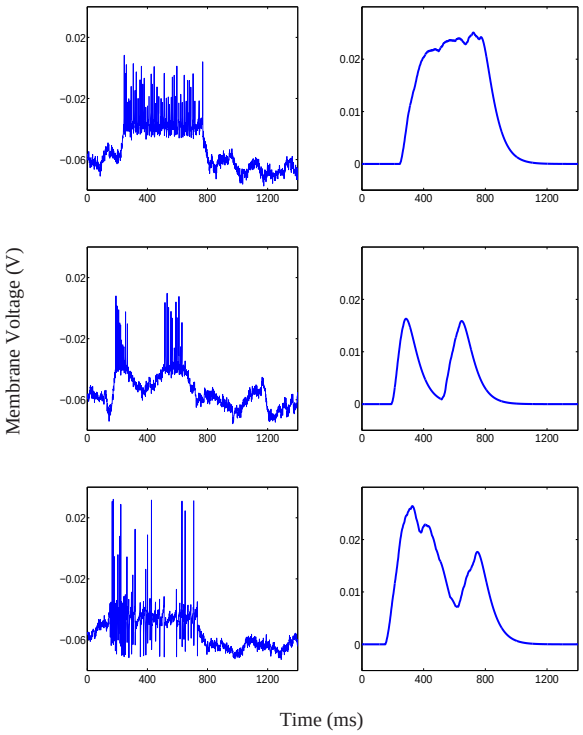

Fig. 13: Responses of model pyramidal cells. The traces in the left column show voltage traces from three model pyramidal cells. The traces in the right column show the smoothed spike rate of the same three cells.

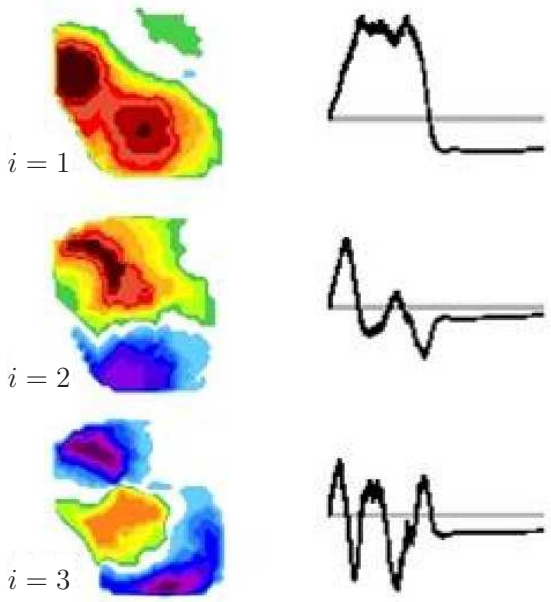

Fig. 14: The left hand column shows the three principal spatial modes. The right hand column shows the corresponding time coefficients.

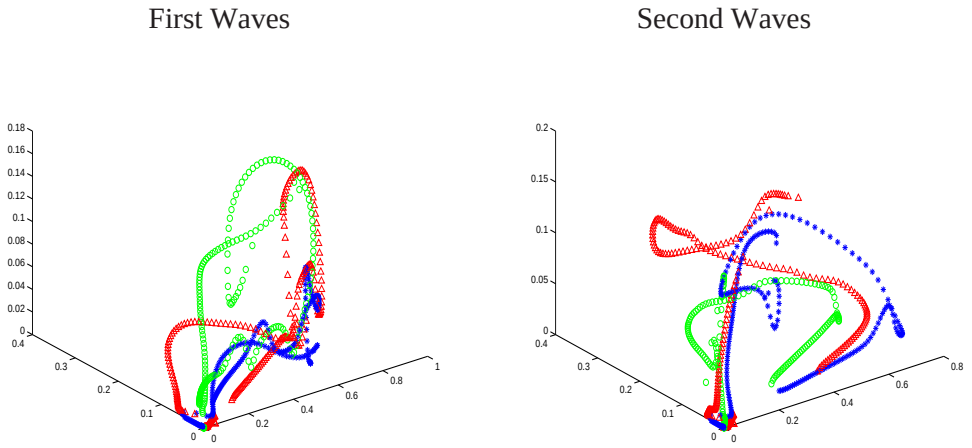

Fig. 15: The typical β-strands with double KL decomposition. In the left figure are the mean β-strands for the 60 presentations for stimuli presented at the left, center, and right clusters of geniculate neurons in the first time period. In the right figure are the mean β-strands in the second time period. The colors, blue, red and green, represent the actual positions of stimuli at left, center and right clusters of geniculate neurons.

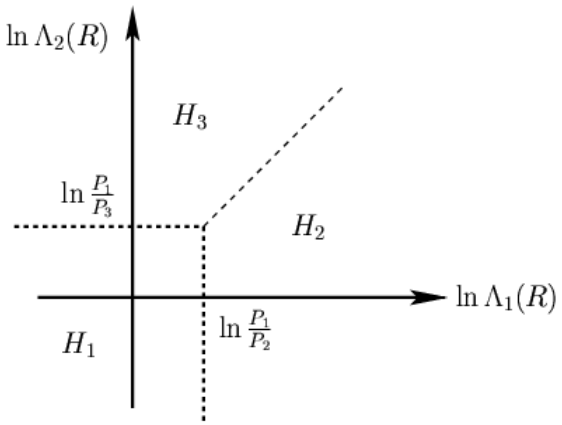

Fig. 16: Decision space divided into three regions, H_1, H_2, and H_3, in terms of the logarithm likelihood ratio (14) and (15). H_1 is the hypothesis that the visual input is from left; H_2 is the hypothesis that the visual input is from center; H_3 is the hypothesis that the visual input is from right. For any give β-strand $r(t)$, the region that the pair $\ln \Lambda_1(R)$ and $\ln \Lambda_2(R)$ fall into in the decision space determines which hypothesis is true.

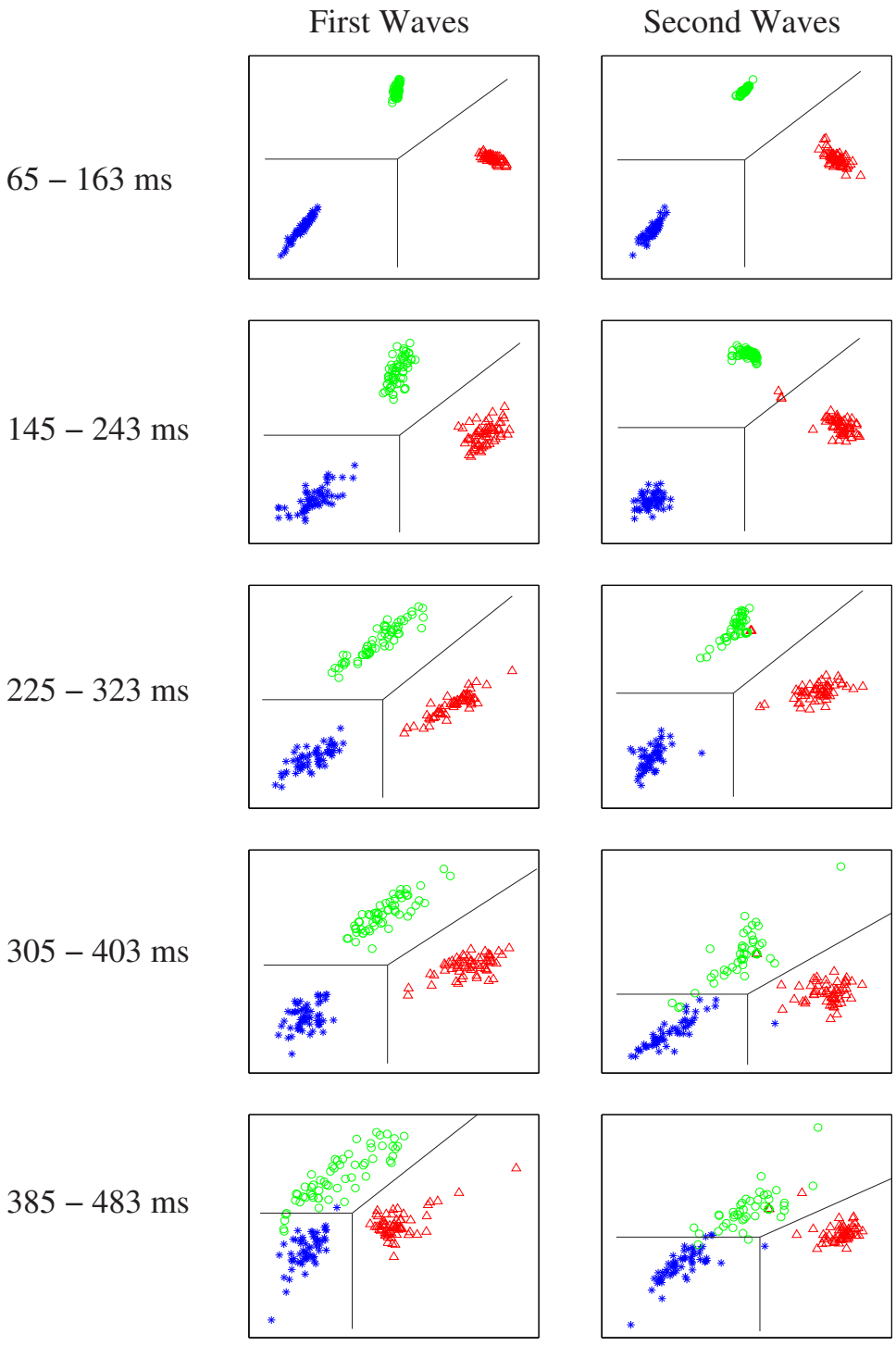

Fig. 17: Decision Spaces for the detection of three hypotheses detection. The coordinates are log likelihood ratios computed for five different time windows. On the left column are the decision spaces using the waves in the first time period and on the right column are the decision spaces using the waves in the second time period. The actual positions of stimuli at left, center and right clusters of geniculate neurons are encoded by the blue, red and green colors respectively.

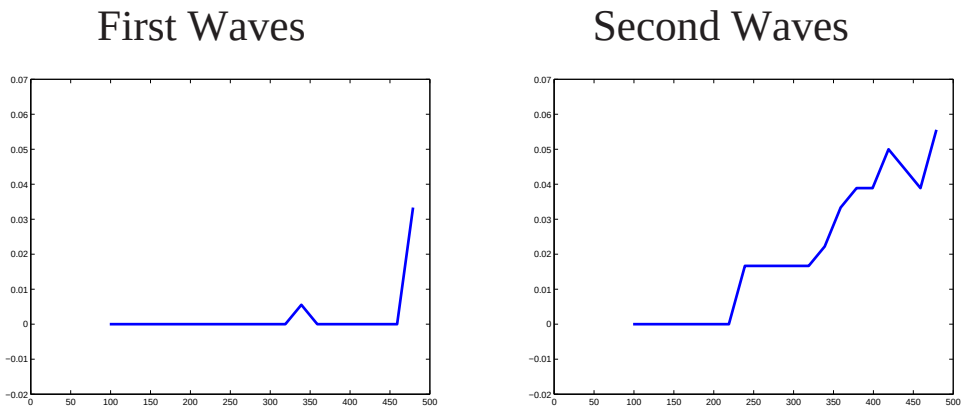

Fig. 18: Detection error probability using statistic method with sliding time window of 99 ms points on β strands. Left figure shows the detection error probability using the first waves and Right figure shows the detection error probability using the second waves.

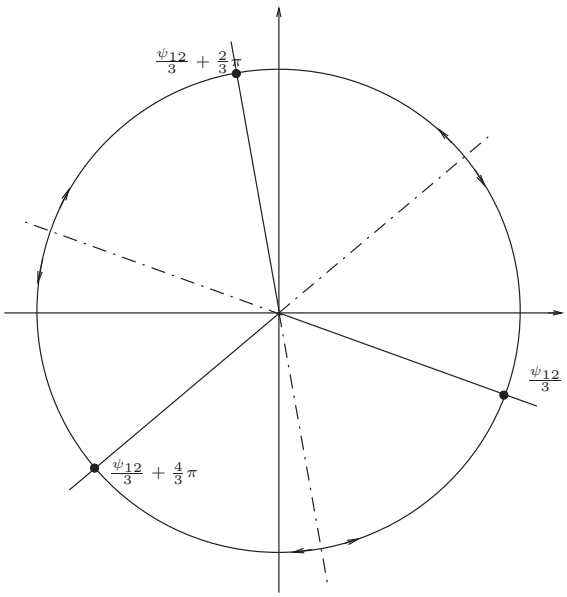

Fig. 19: Phase variable $\bar{\phi}(t)$ is plotted as a unit complex number $e^{i\bar{\phi}(t)}$ with the rescaling parameter 3, showing three stable equilibria which result in three regions of convergence for the dynamical system (22) under initial conditions constrained by (23).

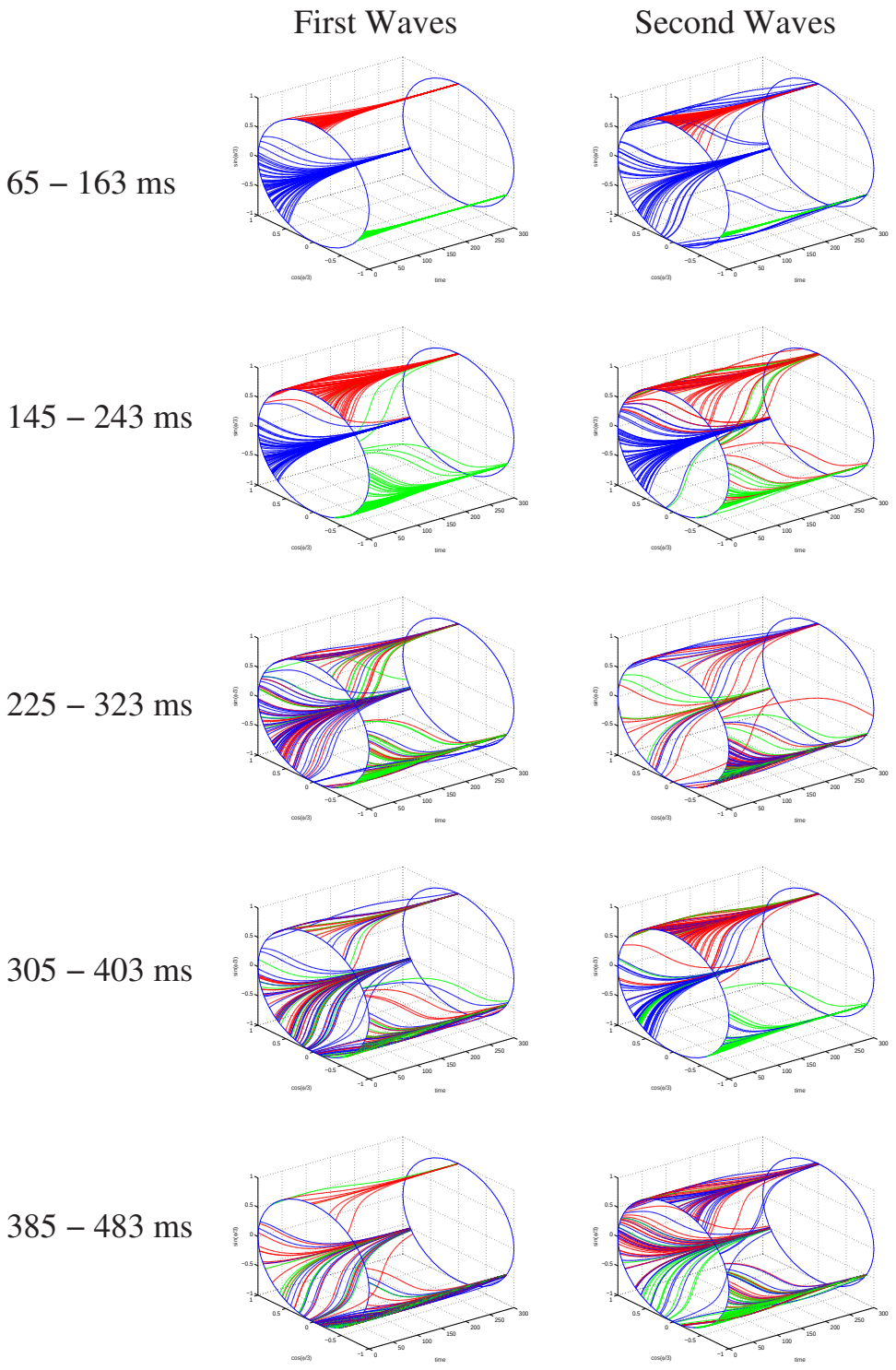

Fig. 20: Convergence of phase variables in the two units Kuramoto model in detection with linear maps from β-space to complex vector space using the first waves and the second waves for five different time windows. The actual positions of stimuli at left, center and right clusters of geniculate neurons are encoded by the blue, red and green colors respectively.

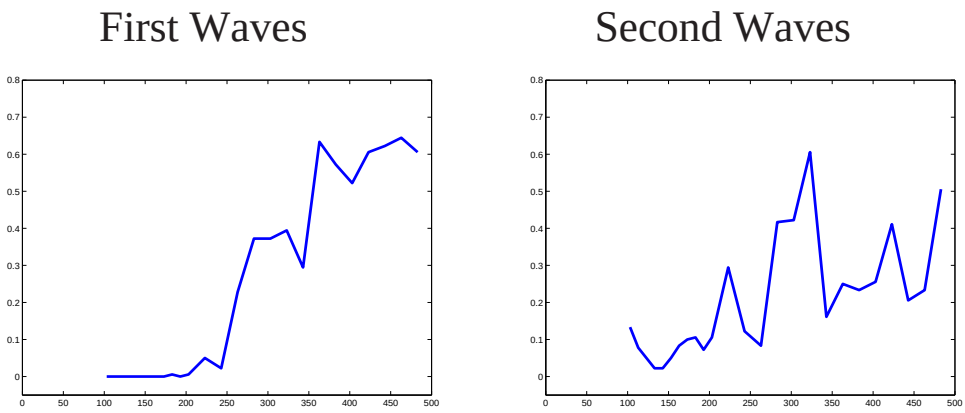

Fig. 21: Detection error probability using Kuramoto Model with points on β strands within sliding time window of 99 ms . Left figure is the detection error probability using the first waves and Right figure is the detection error probability using the second waves.

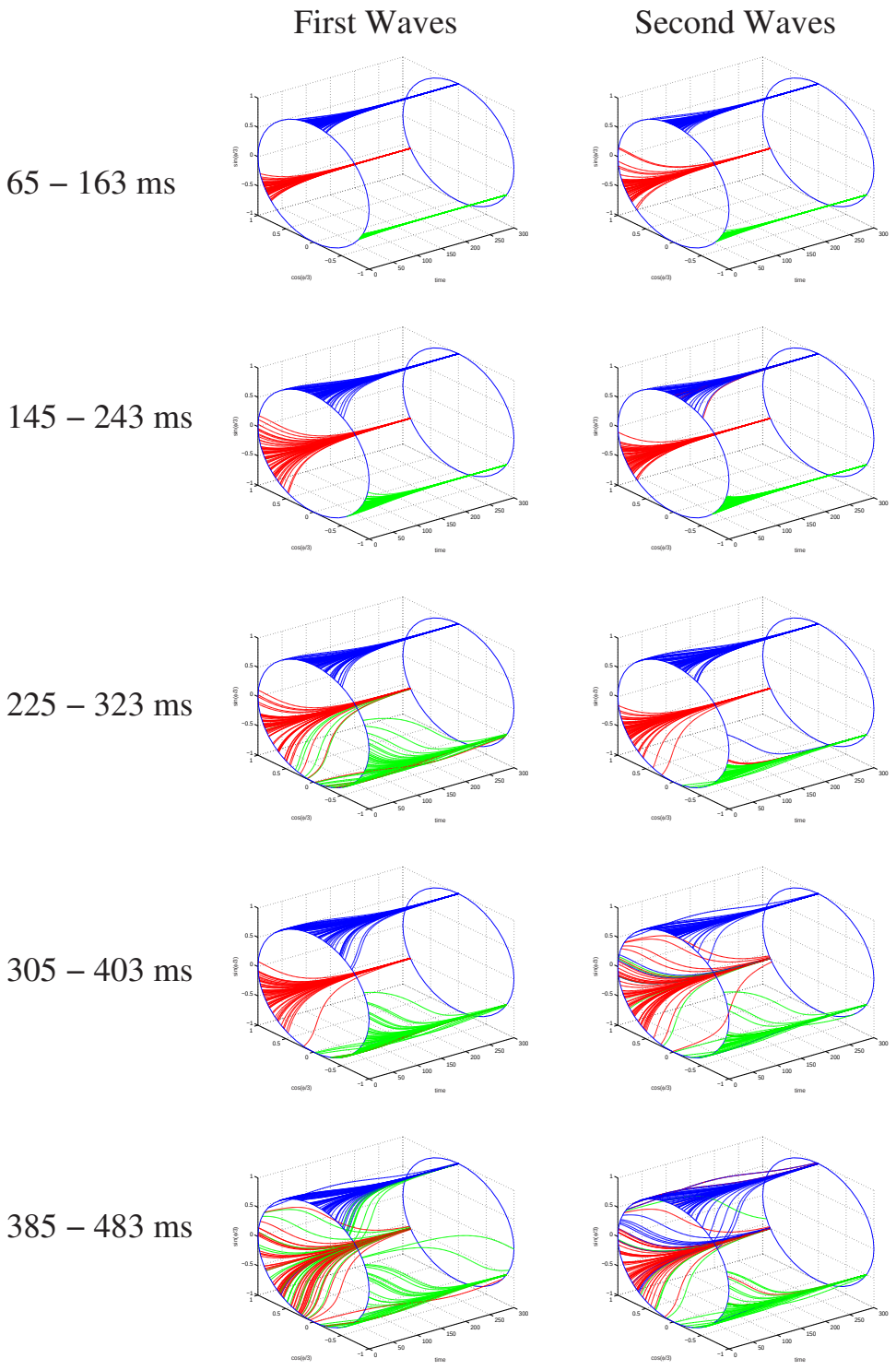

Fig. 22: Convergence of phase variables in the two units Kuramoto model in detection with maps from points in Decision Space to complex vector space using the first waves and the second waves. The actual positions of stimuli at left, center and right clusters of geniculate neurons are encoded by the blue, red and green colors respectively.

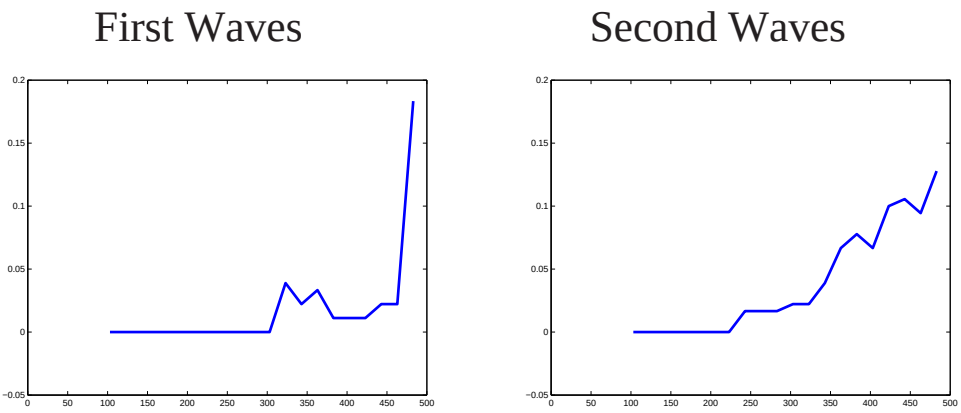

Fig. 23: Detection error probability using Kuramoto Model with maps from points in Decision Space to complex vector space. Left figure is the detection error probability using the first waves and Right figure is the detection error probability using the second waves.